Linear and non-linear inversion schemes to retrieve collision kernel values from droplet size distribution change

Ryo ONISHI[a,], Keigo MATSUDA[b], Keiko TAKAHASHI[a], Ryoichi KUROSE[b], Satoru KOMORI[b]

[a] *Earth Simulator Center, Japan Agency for Marine-Earth Science and Technology, 3173-25 Showa-machi, Kanazawa-ku, Yokohama Kanagawa 236-0001, Japan*
[b] *Department of Mechanical Engineering and Science, and Advanced Research Institute of Fluid Science and Engineering, Kyoto University, Yoshida-honmachi, Sakyo-ku, Kyoto 606-8501, Japan*

Abstract

This study presents an attempt to retrieve collision kernel values from changes in the droplet size distribution due to collision growth. Original linear and nonlinear inversion schemes are presented, which use the simple *a priori* assumption that the total collision rate is given by the sum of the gravitational and turbulent contributions. Our schemes directly handle binned (discretized) size distributions and, therefore, do not require any assumptions on distribution functional forms, such as the self-similarity assumption. To validate the schemes, three-dimensional direct numerical simulation (DNS) of colliding droplets in steady isotropic turbulence is performed. In the DNS, air turbulence is calculated using a pseudo-spectral method, while droplet motions are tracked by the Lagrangian method. Comparison between the retrieved collision kernels and the collision kernels obtained directly from the

Email address: onishi.ryo@jamstec.go.jp (Ryo ONISHI)

DNS show that for low Reynolds number flows both the linear and nonlinear inversion schemes give good accuracy. However, for higher Reynolds number flows the linear inversion scheme gives significantly larger retrieval errors, while the errors for the nonlinear scheme remain small.
Keywords: inversion, collision frequency, particle-immersed turbulence direct numerical simulation

1. Introduction

Collisions of small-inertia droplets are often seen in both environmental and engineering flows. Examples of droplet collisions include the growth of liquid droplets in clouds (Pruppacher and Klett, 1997, Pinsky and Khain, 2002, Shaw, 2003, Wilkinson et al., 2006), in wet steam generators, and in spray atomization processes (Williams and Crane, 1979, Abrahamson, 1975). The collision frequency, N_c, is an important function in those flows, which is expressed as

$$N_c(r_1, r_2) = E_c(r_1, r_2) K_c(r_1, r_2) N(r_1) N(r_2), \tag{1}$$

where r_1 and r_2 are the droplet radii of the colliding droplets, N is the droplet number density, and E_c and K_c are the collision efficiency and collision kernel, respectively. The collision efficiency is the ratio of the number of collisions that occur when the effect of the droplets on the carrier flow is taken into account, to the number that would occur if the carrier flow were unperturbed by the presence of the droplets. Many authors have investigated the collision efficiency of two isolated particles settling in a stagnant fluid (Shafrir and Neiburger, 1963, Lin and Lee, 1975, Davis and Sartor, 1967, Klett and Davis, 1973). However, in more general flows the effect of

the aerodynamic obstruction caused by the droplets is a highly nonlinear problem and there still remain many issues to be resolved, particularly for time-evolving turbulent flows. For this reason, many authors simplify the problem by assuming the collision efficiency in turbulent flows to be unity (Zhou et al., 2001, Riemer and Wexler, 2005).

It is well-known that not all droplet collisions result in a permanent union by coalescence. Thus, a more relevant quantity for real applications is the coalescence (collection) frequency, N_{coal}:

$$\begin{aligned} N_{coal}(r_1, r_2) &= K_{coal}(r_1, r_2) N(r_1) N(r_2) \\ &= E_{coal}(r_1, r_2) N_c(r_1, r_2) \end{aligned} \tag{2}$$

where K_{coal} is the coalescence kernel and E_{coal} is the coalescence efficiency, which is the ratio of number of coalesced pairs to that of collided pairs. The collision kernels, K_c, for particles in turbulent flows have been intensively investigated using both analytical and numerical techniques (Zhou et al., 2001, Saffman and Turner, 1956, Sundaram and Collins, 1997, Kruis and Kusters, 1997, Falkovich et al., 2002, Onishi and Komori, 2004). However, these studies have not gone on to consider E_{coal}. On the other hand, laboratory measurements can access K_{coal}, which contains the total effect of K_c, E_c and E_{coal}. Comparison between K_{coal} from measurements and $E_c \times K_c$ from past theoretical studies will enable us to discuss E_{coal}. So far, laboratory measurements have been restricted to collisions between large and small droplets (Jonas and Goldsmith, 1972, Neizvestnaya and Kobzuenko, 1986).

To measure the collisions among same-sized droplets, we have to generate a spray with mono-dispersed droplets. Unfortunately, there is currently no ideal atomizer capable of spraying vast quantities of droplets of the same

size. Therefore, we are forced to conduct an experiment using a spray with a spread of droplet sizes. To estimate the collision frequencies from the measurements, we are then required to solve an inverse problem, i.e. to retrieve the collision frequencies that give rise to the observed evolution of the drop size distribution. Such inverse techniques are used widely in science and engineering; for example, to deduce geophysical properties from the propagation of seismic waves, to deduce tissue structure from CT scans, and to retrieve CO_2 surface fluxes from observed CO_2 concentrations (Patra et al., 2006).

However, few attempts have been made to apply inverse analysis to retrieve collision frequencies from a temporal change of droplet size distribution. An inverse analysis by Ramkrishna (2000) and co-workers, which is based on the concept of self-similar solutions, is an exception. The self-similarity in size distribution $n_p(m,t)$, where m is the droplet mass, is described by

$$n_p(m,t) = f(z), \tag{3}$$

where z is a similarity variable representing some combination of m and t, e.g., $z = m\phi(t)$ (Muralidhar and Ramkrishna, 1986). The inverse analysis has been applied to both simulated and experimental data for agglomerations (Muralidhar and Ramkrishna, 1986, 1989, Wright and Ramkrishna, 1992, Ramkrishna and Mahoney, 2002) and emulsions (Raikar et al., 2006) in stirred liquid-liquid batch vessels, where self-similar behavior is observed in aged distributions. The similarity assumption is not a common way in size distribution measurements of colliding inertia droplets in air turbulence. It is difficult to hold a group of droplets in a turbulent-air parcel to observe the aged distributions. For example, a group of droplets goes out from the

test section quickly in wind tunnel experiments, and adhesions of droplets on walls cannot be neglected in grid-tank experiments.

We therefore aim to develop and validate inversion schemes to retrieve collision kernel parameters from size distribution changes due to collision growth without assuming self-similarity. Note that we are not targeting the general functional forms for the collision kernels; we start with simplified models of the kernel function, and retrieve suitable values for the model parameters. Our past study proposed a linear scheme and validated it in a low Reynolds flow (Onishi et al., 2008). This study proposes a nonlinear scheme in addition and validates both linear and nonlinear schemes in different Reynolds flows.

To validate the schemes, three-dimensional direct numerical simulation (DNS) of colliding droplets in steady isotropic turbulence was performed, and the size distribution changes due to collisions obtained, together with reference collision kernels. Since it is still computationally impractical to calculate the rebounding of colliding droplets, in the simulation all collisions lead to coalescence; that is, we assume E_{coal} to be unity. As in previous studies (Zhou et al., 2001, Riemer and Wexler, 2005) we assume for simplicity that $E_c = 1$.

The size distribution changes computed in the DNS were used by the inversion schemes to retrieve collision kernels, and the retrieved kernels compared with the reference DNS data. In the next section, we present the formulations of our linear and nonlinear inversion schemes. Simple *a priori* information, based on the idea that the total collision rate is given by the sum of the gravitational and turbulent contributions, is proposed for the schemes. A brief review of inverse analysis for agglomerations in liquid-liquid

system, for specifying the difference between the current and past researches, is shown in § 2.4. The details of the DNS are presented in § 3, and the reliability of our inversion schemes discussed in § 4. Finally, main conclusions are drawn in § 5.

2. Inversion schemes

2.1. Stochastic collection equation (SCE)

The equation for the collision-coalescence growth of droplets can be written in the stochastic collection equation (SCE):

$$\frac{\partial n_p(m,t)}{\partial t} = \int_0^{m/2} K_c(m-m',m') n_p(m-m',t) n_p(m',t) dm' - \int_0^{\infty} K_c(m,m') n_p(m,t) n_p(m',t) dm', \quad (4)$$

where m is the droplet mass, n_p is the number density function, and $K_c(m_a, m_b)$ is the collision kernel between droplets of mass m_a and m_b. The term $n_p(m,t)dm$ denotes the number of droplets per unit volume at time t with mass ranging from $m - dm/2$ to $m + dm/2$. Although the coalescence frequency kernel, K_{coal}, should be used instead of K_c in (4), this study uses K_c instead of the total product of $E_{coal}E_cK_c$ $(= K_{coal})$ since numerical simulations have difficulties in accessing the values of E_{coal} and E_c. However, note that the inversion schemes developed here are not based on the assumptions of $E_{coal} = 1$ and $E_c = 1$.

The SCE is often coupled with turbulence calculation based on the filtered (averaged) Navier-Stokes equations, such as Reynolds-averaged Navier-Stokes (RANS) models and large-eddy simulation (LES) models. Then, the SCE should be averaged and the terms should be represented, e.g., as $<n_p>$,

where $< >$ denotes the averaged value. One should note that the product $<K_c n_{p,1} n_{p,2}>$ is not $<K_c><n_{p,1}><n_{p,2}>$ but G_{12} $<K_c><n_{p,1}><n_{p,2}>$, where G_{12} shows the clustering effect. If we renormalize the collision kernel as $<K_c^*>= G_{12}$ $<K_c>$, we obtain the averaged SCE in the similar form as in (4). In this study, we do not specify the averaging and renormalizations, and simply express terms, e.g., as K_c instead of $<K_c^*>$. It should be mentioned again that K_c implies the total product of $E_{coal} E_c K_c$ $(= K_{coal})$ in this study. Khain et al. (2007) pointed out that there are correlations in $G_{12} E_c$ and $K_c E_c$ under turbulent conditions and that the product $E_c K_c n_{p,1} n_{p,2}$ should be averaged as a whole, i.e., the value of $<E_c K_c n_{p,1} n_{p,2}>$ should be calculated. This fact may invalidate the use of renormalized SCE and reduce the reliability of the present inversions. We have to carefully investigate this issue when we explicitly consider E_{coal} and E_c in future.

When discretizing the droplet size distribution, it is convenient to use an exponential form because the size growth is usually slow among small droplets and fast among large droplets. Berry (1967) introduced the mass distribution function defined as

$$g(y,t)dy = n_p(m,t)mdm, \tag{5}$$

where $y = \ln r$. Using the mass distribution function, (4) is rewritten as

$$\begin{aligned} \frac{\partial g(y,t)}{\partial t} &= \int_{-\infty}^{y_h} \frac{m^2}{m''^2 m'} K_c(y'',y') g(y'',t) g(y',t) dy' \\ &\quad - \int_{-\infty}^{\infty} K_c(y,y') g(y,t) g(y',t) dy', \end{aligned} \tag{6}$$

where y'' is the value for a droplet with mass $m - m'$, and y_h the value for a droplet with mass $m/2$. Berry (1967) also used the equal-ratio form for

discretizing mass:

$$m_l = 2^{1/s} \times m_{l-1}, \tag{7}$$

where s is an integer. This discretization is interpreted as

$$y_l = y_{l-1} + \Delta y, \tag{8}$$

where $\Delta y = (\ln 2)/3s$. In this study, s was set to 4, and 73 bins were used for discretizing the droplet size. The minimum bin had $r_1 = 3.0 \times 10^{-6}$m ($y_1 = -12.7$) and the maximum one had $r_{73} = 1.92 \times 10^{-4}$m ($y_{73} = -8.56$).

The linear flux method (LFM), which is one of the upstream flux methods (UFM) proposed by Bott (1998), is adopted to solve the discretized SCE in this study. Figure 1 shows a schematic illustration of the UFM, where M_i denotes the total mass of droplets with mass ranging from $m_i - dm_i/2$ to $m_i + dm_i/2$. Due to the collision of droplets in grid box i with those in grid box j ($i \leq j$), new droplets with mass $m'(i,j) = m_i + m_j$ are produced.

$$\Delta M' = -\left(\Delta M_i + \Delta M_j\right). \tag{9}$$

Usually, $m'(i,j)$ differs from the discretized mass points m_μ. Instead, one has

$$m_\mu \leq m'(i,j) < m_{\mu+1}. \tag{10}$$

Thus the mass change $\Delta M'$ has to be split into grid boxes μ and $\mu+1$. First, $\Delta M'$ is entirely added to grid box μ, yielding

$$M'_\mu = M_\mu(t) + \Delta M'. \tag{11}$$

Then, a certain fraction of the new mass, $F_{\mu+1/2}$, is transported into grid box $\mu + 1$. This step is written as

$$M_\mu(t + \Delta T) \;=\; M'_\mu - F_{\mu+1/2}(i,j), \tag{12}$$

$$M_{\mu+1}(t+\Delta T) \;=\; M_{\mu+1}(t) + F_{\mu+1/2}(i,j),$$

where $F_{\mu+1/2}/\Delta T$ is the mass flux through the boundary $\mu+1/2$. In UFM, an upstream formula is used for calculating $F_{\mu+1/2}$. The simplest approach is the linear flux method (LFM), where $F_{\mu+1/2}$ is calculated in a linear form as

$$F_{\mu+1/2} \;=\; c_\mu(i,j)\Delta M', \tag{13}$$

where $c_\mu(i,j)$ is interpreted as a Courant number calculated from

$$c_\mu(i,j) \;=\; \frac{m'(i,j)-m_\mu}{m_{\mu+1}-m_\mu}. \tag{14}$$

If we rewrite the above equations with the mass distribution function, g_l $(= g(y_l))$, defined in (5), its change Δg_l in time ΔT is calculated as

$$\begin{aligned}
\Delta g_i &= -g_i\frac{g_j}{m_j}K_c(i,j)\Delta y\Delta T,\\
\Delta g_j &= -g_j\frac{g_i}{m_i}K_c(i,j)\Delta y\Delta T,\\
\Delta g_\mu &= (1-c_\mu(i,j))\; g_ig_j\frac{m'(i,j)}{m_im_j}K_c(i,j)\Delta y\Delta T,\\
\Delta g_{\mu+1} &= c_\mu(i,j)\; g_ig_j\frac{m'(i,j)}{m_im_j}K_c(i,j)\Delta y\Delta T
\end{aligned} \tag{15}$$

where $j>i$. In the special case of $i=j$, the influenced grid boxes are only i and $i+s$, where s is the integer defined in (7), since $m_{i+s}=2\times m_i$. Their temporal changes are calculated as

$$\begin{aligned}
\Delta g_i &= -\frac{g_i^2}{m_i}K_c(i,i)\Delta y\Delta T,\\
\Delta g_{i+s} &= \frac{g_i^2}{m_i}K_c(i,i)\Delta y\Delta T.
\end{aligned} \tag{16}$$

The LFM is referred to as a bin-based pair-interaction method in Wang et al. (2007), which reported an intensive investigation on the accuracy and convergence properties of the collection equation solvers. Wang et al. (2007) classified the solvers into three groups; the first group is denoted as point-based methods of, for example, Berry and Reinhardt (1974), Gelbard and Seinfeld (1978), Eyre et al. (1988). The second group refers to spectral moment methods pioneered by Bleck (1970), Enukashvily (1980), and further developed by (Tzivion et al., 1987, 1999, 2001). The third group termed as the bin-based pair-interaction methods includes the linear discrete method (LDM) of Simmel et al. (2002) and the bin integral method with Gauss quadrature (BIMGO) of Wang et al. (2007), and the LFM. The basic idea is to break the contributions to the gain and loss integrals as a summation of a series of binary pair-interactions. The loss in i and j bins are converted into the gain in μ and $\mu + 1$ bins as illustrated in figure 1. Therefore, the mass conservation is ensured by design. The inherent problem of LFM is a lack of logical reasoning in redistributing the mass into μ and $\mu+1$ bins. In addition, Wang et al. (2007) pointed out that LFM suffers from numerical diffusion. However, the results of LFM show little difference from the converged solution even in an intermediate bin resolution of s=2 as far as the mass distribution has single peak (see for example figures 6 and 11 in Wang et al. (2007)). This justifies the adoption of LFM in this study, where s=4 is used. The largest reason why we adopt LFM is that the equations (15) and (16) can be written in a linear form using matrices as below, which makes the inversion procedure very simple.

$$\mathbf{d} = \mathbf{G}\mathbf{m}, \tag{17}$$

where $\mathbf{d}$ is the size distribution change vector for a given time interval of ΔT, $\mathbf{m}$ is the collision kernel vector, and $\mathbf{G}$ is the size distribution matrix.

For q droplet size bins, $\mathbf{d}$, $\mathbf{m}$, and $\mathbf{G}$ are defined as $q \times 1$, $q^2 \times 1$ and $q \times q^2$ matrices, respectively:

$$\mathbf{d} = \left[\Delta g_1, \Delta g_2, \cdots, \Delta g_k, \cdots, \Delta g_q\right]^T, \tag{18}$$

$$\mathbf{m} = \left[K_c(1,1), K_c(1,2) \cdots, K_c(i,j), \cdots, K_c(q,q)\right]^T, \tag{19}$$

$$\mathbf{G}(t, \Delta T) = \left[\mathbf{G}_1, \mathbf{G}_2, \cdots, \mathbf{G}_k, \cdots, \mathbf{G}_q\right]^T. \tag{20}$$

Here $\mathbf{G}_k$ is a $1 \times q^2$ matrix defined as

$$\mathbf{G}_k = \left[G_k(1,1), G_k(1,2) \cdots, G_k(i,j), \cdots, G_k(q,q)\right], \tag{21}$$

where $G_k(i,j)$ shows the mass change in grid box k due to droplet collisions between grid boxes i and j. Equations (15) and (16) are rewritten respectively as

$$\begin{aligned}
G_i(i,j) &= -g_i \frac{g_j}{m_j} \Delta y \Delta T, \\
G_j(i,j) &= -g_j \frac{g_i}{m_i} \Delta y \Delta T, \\
G_\mu(i,j) &= \left(1 - c_\mu(i,j)\right)\, g_i g_j \frac{m'(i,j)}{m_i m_j} \Delta y \Delta T, \\
G_{\mu+1}(i,j) &= c_\mu(i,j)\, g_i g_j \frac{m'(i,j)}{m_i m_j} \Delta y \Delta T,
\end{aligned} \tag{22}$$

where $j > i$, and

$$
\begin{aligned}
G_i(i,i) &= -\frac{g_i^2}{m_i}\Delta y \Delta T, \\
G_{i+s}(i,i) &= \frac{g_i^2}{m_i}\Delta y \Delta T,
\end{aligned}
\tag{23}
$$

in the special case of $i = j$. The following equation may be easier to read than (17).

$$
\begin{aligned}
\Delta g_k &= \mathbf{G}_k \mathbf{m} \\
&= \sum_{i,j} G_k(i,j) K_c(i,j).
\end{aligned}
\tag{24}
$$

If we use the indicial notation, equation (17) is rewritten as

$$
d_k = G_{ijk} m_{ij}, \tag{25}
$$

where d_k, m_{ij} and G_{ijk} have q, q^2 and q^3 dimensions, respectively. Equations (18) - (21) are then rewritten as follows.

$$
d_k = \Delta g_k, \tag{26}
$$

$$
m_{ij} = K_c(i,j), \tag{27}
$$

$$
G_{ijk} = G_k(i,j), \tag{28}
$$

where $G_k(i,j)$ is defined in (23).

2.2. Linear inversion scheme

Basic formulations for linear inversion scheme are described in Onishi et al. (2008). Here we rewrite the formulations in more detail. If the size distribution matrix, $\mathbf{G}$, and collision kernel vector, $\mathbf{m}$, are given, then the size distribution change vector during a given time, $\mathbf{d}$, can be calculated from (17). This is the physically-forward procedure. In contrast, calculating $\mathbf{m}$ from a given $\mathbf{G}$ and $\mathbf{d}$ is an inverse procedure, which is targeted in this study.

The dimension of target vector $\mathbf{m}$ (the collision kernel vector) is of $(q^2 + q)/2$ degrees of freedom, which is larger than the number of conditional equations in (17). That is, the inverse problem discussed here is underdetermined. Therefore, we need to introduce *a priori* information. We assume that droplet collisions can be expressed by the sum of the collisions due to the settling velocity difference (the gravitational contribution) and those due to turbulence (the turbulence contribution) (Zhou et al., 2001, Falkovich et al., 2002). The model for gravitational collision is called the hydrodynamic kernel model:

$$K_{c,hydr}(i,j) = \pi R^2 \left| V_\infty(m_i) - V_\infty(m_j) \right|, \tag{29}$$

where $V_\infty(m)$ is the gravitational settling velocity of droplets with mass m, and $R(= r_i + r_j)$ is the collision radius. For the collisions induced by turbulence, Saffman and Turner (1956) have proposed a turbulent collision kernel model applicable to small Stokes number, St, which is the ratio between the particle relaxation time, τ_p, to the Kolmogorov dissipation time, τ_η.

$$\begin{aligned} St &= \frac{\tau_p}{\tau_\eta} \\ &= \frac{2\rho_p}{9\rho_f} \left(\frac{r}{l_\eta} \right)^2, \end{aligned} \tag{30}$$

where ρ_p and ρ_f are the densities of particle and fluid, respectively, and l_η is the Kolmogorov dissipation scale. The collision kernel of Saffman and Turner (1956) is expressed as

$$K_{c,ST}(i,j) = \sqrt{\frac{8\pi}{15}}\lambda R^3, \tag{31}$$

where the local shear rate, λ, is defined by the energy dissipation rate, ϵ, and kinematic viscosity, ν as $\lambda = (\epsilon/\nu)^{1/2}$. The *a priori* information is then written in a linear form as

$$K_c(i,j) = K^*_{c,hydr}(i,j) + k_t K^*_{c,ST}(i,j). \tag{32}$$

Although the kernel (31) is valid only for small inertia droplets in theory, the insufficiency can be compensated by k_t. Here, k_t is not a constant but a variable depending on the system. For example, k_t depends on flow Reynolds numbers and droplet size distributions as well. This is the key of the present *a priori* information. Despite their simplicity, these *a priori* assumptions give good results, as shown in the discussion section.

The first term in the rhs of (32) represents the gravitational contribution and the second one the turbulent contribution. A linear form is used in (32) in order to combine the two contributions, although the root-mean-square (RMS) form is often used (Wang et al., 1998, Dodin and Elperin, 2002, Onishi, 2005). The linear form enables us to perform a linear inversion. Instead, the linear form tends to overestimate the total collision kernel when the two contributions are close in magnitude. For reducing this problem, we use a switching technique based on the idea that the gravitational contribution is relatively dominant for large size difference; the following $K^*_{c,hydr}$ and $K^*_{c,ST}$

are used in (32) instead of $K_{c,hydr}$ and $K_{c,ST}$.

$$
\begin{aligned}
K^*_{c,hydr}(i,j) &= \begin{cases} 0, & r^{\#}_{diff} < C_t \\ K_{c,hydr}(i,j), & \text{otherwise.} \end{cases} \\
K^*_{c,ST}(i,j) &= \begin{cases} \lambda R^3, & r^{\#}_{diff} < C_t \\ 0, & \text{otherwise.} \end{cases}
\end{aligned} \tag{33}
$$

Here, $r^{\#}_{diff} = \frac{|r_i - r_j|}{(r_i + r_j)/2}$ and C_t is a threshold. The available value of C_t ranges $0 < C_t \leq 2$ since $0 \leq r^{\#}_{diff} \leq 2$. In this study, C_t is set at 0.5 although it should be determined depending on the target system. A discussion on C_t is shown in section 4.4.

Using the *a priori* information, the collision kernel vector $\mathbf{m}$ can be rewritten as

$$
\begin{aligned}
\mathbf{m} &= \left[K^*_{c,hydr}(1,1), K^*_{c,hydr}(1,2), \cdots, K^*_{c,hydr}(q,q)\right]^T \\
&\quad + k_t \left[K^*_{c,ST}(1,1), K^*_{c,ST}(1,2), \cdots, K^*_{c,ST}(q,q)\right]^T \\
&= \mathbf{m}_{hydr} + k_t \mathbf{m}_{ST}.
\end{aligned} \tag{34}
$$

Then (17) can be rewritten as

$$
\mathbf{d}' = \mathbf{G}' \cdot k_t, \tag{35}
$$

where $\mathbf{d}' = \mathbf{d} - \mathbf{G}\mathbf{m}_{hydr}$ and $\mathbf{G}' = \mathbf{G}\mathbf{m}_{ST}$. It should be noted that k_t is the only unknown value in (35).

Bins with larger numbers of droplets have more information for analysis. As an extreme example, if a bin has no droplets, the bin has no importance for collisions. In order to consider this, we introduce a weighting matrix,

which has diagonal sections proportional to the square of the droplet number densities;

$$\mathrm{diag}(\mathbf{W_e}) = \left[n^2_{p,ave}(m_1), \cdots, n^2_{p,ave}(m_q)\right], \tag{36}$$

where $n_{p,ave}$ is the average of the number density functions before and after collision growth. Finally, the least-square method retrieves the value of k_t as

$$k_t = \left[\mathbf{G'}^T \mathbf{W_e} \mathbf{G'}\right]^{-1} \mathbf{G'}^T \mathbf{W_e} \mathbf{d'}. \tag{37}$$

2.3. Nonlinear inversion scheme

In the linear inversion, we implicitly assume that the size distribution does not change for ΔT. This assumption is needed to consider the collision growth as a linear phenomenon. However, this assumption is not required in nonlinear inversion. In nonlinear inversion, ΔT can be divided into M sub-steps.

$$\begin{aligned} \mathbf{d} &= \sum_{\mu=0}^{M-1} \mathbf{d}_\mu \\ &= \sum_{\mu=0}^{M-1} \mathbf{G}(t_\mu, \Delta T/M)\mathbf{m}, \end{aligned} \tag{38}$$

where $t_{\mu+1} = t_\mu + \Delta T/M$. Of course, a larger M provides a more accurate calculation. In the present nonlinear scheme, M was set to 20.

In our nonlinear inversion scheme, the optimal value of k_t is searched iteratively. Initially, the size distribution change, $\mathbf{d}$, is calculated using a collision kernel vector, $\mathbf{m}^0$, determined from a certain k_t^0. The bias between the calculated size distribution change, $\mathbf{d}$, and the observed (reference) one, $\mathbf{d}^{obs}$, is evaluated from the evaluation function:

$$\Phi = \left[\mathbf{d} - \mathbf{d}^{obs}\right]^T \mathbf{W_e} \left[\mathbf{d} - \mathbf{d}^{obs}\right]. \tag{39}$$

To obtain the optimal value of k_t, which produces the smallest possible Φ, the Newton-Raphson technique is used:

$$k_t^{p+1} = k_t^p - \alpha \frac{\Phi^p}{\delta\Phi^p/\delta k_t^p}, \tag{40}$$

where k_t^p and Φ^p are the values at p-th iteration, and $\delta\Phi^p = \Phi^p - \Phi^{p-1}$. The acceleration coefficient, α, was set to 5.0×10^{-4} in this study. The iterations were continued until $|\delta\Phi^p/\Phi^p| < 10^{-5}$. We used the value of k_t obtained from the linear inversion, which is calculated from (37), as the initial value, k_t^0.

2.4. Comparison with past inverse analysis in agglomeration kinetics

Muralidhar and Ramkrishna (1986) extracted the agglomeration frequency from self-similar size distributions after the assumption that the agglomeration frequency is homogeneous. The homogeneous kernel has the property

$$K_c(Ar_1, Ar_2) = A^\xi K_c(r_1, r_2), \tag{41}$$

where ξ is the degree of homogeneity. They used the temporal data of total particle density to identify ξ and similarity parameter in equation (3) by means of a least-squares fit. Although, potentially useful, the assumption of homogeneity is drastic. For example, the well-known formula for the small Stokes particles ($St \ll 1$) with gravitational settling is not homogeneous (Saffman and Turner, 1956):

$$\begin{aligned} K_c(r_1, r_2) &= 2\sqrt{2\pi}(r_1 + r_2)^3 \\ &\times \left[\left\{ 1.3 \left(\frac{\epsilon^3}{\nu} \right)^{1/2} + \frac{g^2}{3} \right\} \left(\frac{2\rho_p}{9\nu\rho_f} \right)^2 (r_1 - r_2)^2 + \frac{\epsilon}{9\nu} \right]^{1/2}. \end{aligned} \tag{42}$$

It should be noted that our schemes do not require the homogeneity, and the form of kernel (32) is not homogeneous.

Muralidhar and Ramkrishna (1989) then relaxed the assumption of the homogeneity at the cost of obtaining additional data on the time rate of change of the average particle size. Wright and Ramkrishna (1992) took the advantage of the constraints that similarity places on the agglomeration frequency to simplify the formulation of Muralidhar and Ramkrishna (1989). Recently, Raikar et al. (2006) applied the inversion technique based on the similarity assumption to retrieve a breakage rate in a turbulently agitated batch emulsification vessel. Such agglomeration and emulsion researches using batch vessels observe self-similarity behavior in aged distributions. However, the similarity assumption is not a common way in size measurements of colliding droplets in air turbulence due to a difficulty in holding a group of droplets under observation until it exhibits the similarity. For example, a group of droplets goes out from the test section quickly in wind tunnel experiments, and adhesions of droplets on walls cannot be neglected in grid-tank experiments.

Zauner and Jones (2000) estimates the agglomeration kernel value of precipitating crystals without the similarity assumption from measured size distribution. They performed several forward simulations of evolving size distribution for different values of the agglomeration kernel, and determined the best kernel that produces the most similar evolutions with measurement. In short, they searched the best estimate from trial and errors. In contrast, we develop inversion schemes, which find the best estimates numerically. Our schemes are free from the similarity assumption as well, and, therefore, suit-

able for retrieving collision frequencies of inertia droplets in air turbulence. Our nonlinear scheme instead requires large computational cost, but it is still feasible even with personal computers.

3. Three-dimensional direct numerical simulation (DNS) of steady isotropic turbulence with droplet collisions

We aim to develop the inversion schemes to retrieve collision kernels from the size distribution changes. Although the ultimate goal of this study is to retrieve the collision kernels from laboratory data, we here perform numerical simulations of particle-laden turbulent flows using a three-dimensional DNS instead of laboratory experiments. In the DNS experiments, the size distribution measured in an actual water spray was used as the initial distribution for collision growth simulations.

3.1. Numerical setups

A schematic diagram of a plausible experiment for collision kernel measurement is shown in figure 2. Water droplets are sprayed into a grid-generated turbulent flow. Droplet collision growth then causes differences between the droplet size distributions measured at the upstream and downstream points. The collision growth time T_c is L/U_0, where U_0 is the background mean flow velocity and L is the distance between two measuring points. The sprayed droplets sediment due to gravity and this may cause an inequality of average number concentrations in cross-sectional profiles in such a horizontal wind tunnel. However, if the droplet's size is in the range of cloud droplets' size, i.e. in the order of 10 μm, the gravitational sedimentation is in the order of 10^{-2} m/s. This is three-orders smaller than the

carrier-flow of around 10 m/s. Therefore, the gravitational sedimentation of droplets would not cause a serious problem in the horizontal wind tunnel. The vertical wind-tunnel is, of course, preferable to avoid this problem.

In this study, we used direct numerical simulations (DNS) of particle-laden turbulent flows instead of laboratory experiments. The DNS can reproduce the isotropic turbulence observed in a small wind tunnel similar to that used by Aliseda et al. (2002), who conducted a laboratory experiment using a grid-generated turbulence with a uniform flow of U_0 =10 m/s in a small wind tunnel of 20 cm $\times$ 20 cm $\times$ 2.5 m. They obtained an isotropic turbulence with a Kolmogorov length scale, $l_\eta (= (\nu^3/\epsilon)^{1/4})$, of 2.58×10^{-4} m and a Taylor-microscale based Reynolds number, Re_λ, of 56.3 at 1.68 m behind the turbulence-generating grid. In their small wind tunnel, collision growth measurements for about 0.2 s would be possible because air goes through the tunnel in 0.25 s (=2.5 m / 10 m/s). Therefore, the collision growth time, which refers to the possible duration in a small wind tunnel, was fixed at 0.2 s in the DNS. The initial droplet size distribution was set to the size distribution measured in a water spray from a nozzle-type atomizer. Although the actual grid-generated turbulence decays downstream, we used a simple assumption that the droplets collide and coalesce in a steady isotropic turbulence.

3.2. Flow field

A pseudo-spectral method based on the Fourier-Galerkin method was used to solve three dimensional vorticity equations:

$$\frac{\partial \omega_i}{\partial t} + U_j \frac{\partial \omega_i}{\partial x_j} = \omega_j \frac{\partial U_i}{\partial x_j} + \nu \frac{\partial^2 \omega_i}{\partial x_j \partial x_j} + F_i. \tag{43}$$

	N_g	Re_λ	l_η/L_0	l_I/L_0	$k_{eff}(l_\eta/L_0)$
FLOW-1	64	54.4	0.0538	1.56	1.15
FLOW-2	96	71.3	0.0401	1.60	1.27
FLOW-3	128	83.2	0.0319	1.57	1.36
FLOW-4	128	92.9	0.0271	1.53	1.16

Table 1: Flow conditions and properties in the DNS

Here, U_i is the air velocity in the i-direction, ω_i is the vorticity around the i-axis, and F_i represents an external force. The kinematic viscosity, ν, was set to 1.50 $\times 10^{-5}$ m^2/s at 1 atm and 298 K. The forcing scheme by Squires and Eaton (1991) for the low-wavenumber range was used to generate steady flows. In this scheme, a non-uniform, time-independent, large-scale force field was added to the flow at each time step. The fourth-order Runge-Kutta method was used to simulate time evolutions, while the two-thirds method was used to eliminate aliasing errors. The vorticity equations were discretized on a cubic domain of length $2\pi L_0$, where L_0 is the representative length scale, and periodic boundary conditions were applied in all three directions. The flow cube was discretized uniformly into ${N_g}^3$ grid points. The above fluid calculation method is based on the open source of Ishioka (2005).

Table 1 lists the computational conditions and flow properties. Four airflow simulations (FLOW-1, 2, 3 and 4) were performed. The airflows have different RMS values of velocity fluctuation, u_{rms}, which is controlled by the forcing strength of F_i. The grid resolution for the fluid calculation was set to $N_g = 64$ in FLOW-1, $N_g = 96$ in FLOW-2, and $N_g = 128$ in FLOW-3 and 4, while L_0 was fixed at 5.0 mm in all simulations. The typical turbu-

lence properties of Re_λ, l_η and l_I are the Taylor-microscale based Reynolds number, Kolmogorov length scale and integral length scale, respectively. The maximum effective wavenumber, which is denoted by k_{eff}, was $N_g/3$ since the two-thirds dealiasing was used. It is widely accepted that the product $k_{eff}(l_\eta/L_0)$ should be greater than unity for sufficient resolution at small scales, and the values in table 1 satisfy this criterion. The integral scales represent the artificial forcing scales where energy is added to maintain the steady flows. The integral scales should be sufficiently larger than the Kolmogorov scales since the artificial forcing should not influence the energy dissipation system. The values in table 1 show that the integral scales are more than one order larger than the Kolmogorov scales, and these large scale-separations justify the forcing scheme used in this study. The values of l_η and Re_λ in FLOW-1 were close to those obtained in the small wind tunnel experiment of Aliseda et al. (2002), suggesting that the numerical results from FLOW-1 will be useful when discussing the actual wind tunnel experiments.

3.3. Droplet motion

A water droplet is considered as a Stokes particle with inertia, which is governed by the equation:

$$\frac{\partial V_i}{\partial t} = -\frac{V_i - U_i}{\tau_p} + \delta_{i2} g_r, \tag{44}$$

where V_i is the particle velocity, g_r is the gravitational acceleration, and τ_p is the particle relaxation time defined as

$$\tau_p = \frac{\rho_p}{\rho_f} \frac{2r^2}{9\nu}. \tag{45}$$

The value of ρ_p/ρ_f was set to 8.43×10^2 at 1 atm and 298 K. The second-order Adams-Bashforth method was used for time integration. The flow velocity,

U_i, in (44) at a droplet position is linearly interpolated from the vicinity grid values. The Stokes drag model is used in (45). Strictly speaking, the Stokes drag model is not appropriate for a water droplet with a radius larger than 70 μm because the particle Reynolds number exceeds unity. For simplicity, all droplets in this study were, however, considered as Stokes particles. At the same time, our numerical simulation assumes that particle diameter is negligibly small compared to the Kolmogorov scale, i.e., $2r \ll l_\eta$. Bagchi and Balachandar (2003) reported that the reliability of standard drag model decreases with increasing particle size when $2r \sim l_\eta$. Actually, the largest particle diameter considered is around the Kolmogorov scale. However, its number density is enough small to validate the neglect of the large particle problem.

3.4. Droplet collision growth

To perform collision growth calculations in realistic conditions, we used the size distribution which was measured in a water spray from a nozzle-type atomizer by using a Phase Doppler Anemometry (58N80-SYSTEM, DANTEC inc.) as the initial distribution in our DNS.

Figure 3 shows the measured size distribution (bold solid line) and the corresponding number densities used in the DNS for each sized droplet (vertical bars). The number densities were used for the initial droplet sizes in the DNS. The left vertical axis is for the solid line and the right one is for the bars, while the horizontal axis shows the droplet radius in μm. The most frequent radius, r_{freq}, of the size distribution is 39.0 μm with a number-average radius, r_{ave}, of 48.3 μm and a standard deviation of 33.3 %. In the DNS, 4096 water droplets with the number densities as demonstrated by the bars were initially

randomly located in the computational domain. The droplets had radii with 1 μm steps, such as 38.0 μm, 39.0 μm and 40.0 μm. It should be noted that the droplets are calculated with a Lagrangian-tracking scheme in the DNS, and with an Eulerian-in-radius discretization scheme in inversions. In the inversions, the droplet sizes are discretized in (8). The total number density of the water droplets was $4096/V_d (= 1.32 \times 10^8$ m$^{-3})$, where $V_d (= (2\pi L_0)^3)$ is the volume of domain. The particle volume and mass fractions had so small values of 8.46×10^{-5} and 7.13×10^{-2}, respectively. Turbulence modulation by droplets was, therefore, assumed to be negligibly small because of the dilute condition.

To remove the influence of the initial conditions, the droplet motion was initially calculated with elastic collisions, and without coalescences, for three times the flow integral time, $T_e (= l_I/u_{rms})$. After this "spin-up" computation, droplets were allowed to grow by geometric collision-coalescences. We set $t = 0$ as the time when coalescence begins. The collision growth simulations were carried out for a fixed duration of 0.2 s, as determined in § 3.1. For each flow condition, ten collision-growth runs with different initial flow conditions were performed, and the obtained size distributions were averaged.

3.5. Reference collision kernels

In order to obtain the reference collision kernels, additional DNS calculations were carried out. In those DNS calculations, 2048 particles with radius r_1 and 2048 particles with radius r_2 were distributed into steady isotropic turbulence, and their geometric collisions counted (Onishi et al., 2009).

Three sets of collisions are detected in each calculation; one is the collisions among r_1 particles, second among r_2 particles (collisions among mono-

dispersed particles), and third is those between r_1 and r_2 particles (collisions between bi-dispersed particles). Providing the number of those collisions at the n-th time step are $N^n_{col,11}$, $N^n_{col,22}$ and $N^n_{col,12}$, the collision kernels, $K^n_{c,11}$, $K^n_{c,22}$ and $K^n_{c,12}$, were calculated as

$$K^n_{c,11} = \frac{1}{2N(r_1)N(r_1)} \times \frac{N^n_{col,11}}{V_d \Delta t}, \tag{46}$$
$$K^n_{c,22} = \frac{1}{2N(r_2)N(r_2)} \times \frac{N^n_{col,22}}{V_d \Delta t},$$
$$K^n_{c,12} = \frac{1}{N(r_1)N(r_2)} \times \frac{N^n_{col,12}}{V_d \Delta t},$$

where Δt is the computational time step. The mean collision kernels were calculated by averaging the collision kernels at each time step.

4. Results and discussion

4.1. Droplet collision growth by DNS

Figure 4(a) shows the non-dimensionalized energy spectra of air turbulence. The horizontal axis is the non-dimensionalized wave number. Each curve has the -5/3 power law slope in the inertia subrange. It is clearer in higher Reynolds flow. Figure 4(b) shows a snapshot of the three-dimensional velocity vectors and droplet positions in FLOW-1. The velocity vectors on the plane of $z/L_0 = \pi$ are drawn with arrows, and droplets magnified by a factor of six are plotted. Figure 4(a) and (b) confirm that the airflow is in a fully turbulent state and the droplets are randomly distributed.

Figure 5 shows the droplet size distributions obtained by the collision growth simulation in FLOW-1. The initial size distribution, which was determined in § 3.4, is shown as a solid line. The DNS prediction at t^*(=

$t/T_e) = 5.1$, i.e., after the collision growth, is shown as a dashed line. Due to the collision growth, the number of droplets decreases and becomes 3508.5 on ten-run average, which is 14 % smaller than the initial number of 4096. The average radius increases and becomes 50.2 μm, which is 3.9 % larger than the initial value of 48.3 μm. The most frequent radius does not increase although the average radius does. This indicates the size distributions are not self-similar since equation (3) is not satisfied.

If we neglect the size deviation in the initial size distribution and assume that all the droplets have the same radius r_{freq} (=39.0 μm) , we can roughly estimate a collision kernel from the change in number of droplets as follows: Average number density N_{ave} for a duration of collision growth T_c is $N_{ave} = (\zeta_0 + \zeta_{end})/2/V_d$, where ζ_0 is the initial number of droplets in the domain and ζ_{end} the number after the collision growth. Number of collisions in the domain for T_c, N_{col}, is $(\zeta_0 - \zeta_{end})$ if multiple collisions are neglected. Then, the rough estimation of collision kernel among r_{freq} droplets is calculated as

$$K_c^{est}(r_{freq}, r_{freq}) = \frac{1}{2N_{ave}^2} \times \frac{N_{col}}{V_d T_c} \tag{47}$$

For example, a normalized collision kernel $K_c^{est}(r_{freq}, r_{freq})/\lambda R^3$ in FLOW-1, where r_{freq}=39.0 μm, $T_c = 0.2$ s, ζ_0=4096 and ζ_{end}=3508.5, is estimated to be 32.4. The reference collision kernel obtained from the DNS is 42.2, showing that the rough estimation has as much as 23 % error.

4.2. Retrieved collision kernels

Substituting the retrieved value of k_t, collision kernels can be obtained from (32). To validate the reliability of our inversion schemes, the retrieved collision kernels were compared with the DNS reference data.

Figure 6 shows the collision kernels retrieved by the present inversion schemes, together with the collision kernels obtained by the DNS of monodispersed droplets for a number of choices of the droplet size. The vertical axis shows the collision kernels normalized by the local shear rate, λ, and the collision radius, $R(=2r)$, and the horizontal axis shows the droplet radius and Stokes numbers. Solid circles are the DNS data, while the solid and dashed lines are the collision kernels retrieved by the linear and nonlinear inversions, respectively. Hereafter, collision kernels retrieved by the linear scheme are referred to as Kc-L, while those by the nonlinear scheme are referred to as Kc-NL. Figure 6 shows the inconsistencies of distributions in shape; the DNS data show a continuous decrease, whereas the retrieved ones are constants. The point to be noticed here is, however, that the retrieved values are close to the DNS data around r_{freq}, where the largest available information on collisions is contained. As shown in figure 5, the size of droplets ranges from 20 μm to 100 μm. Those droplets were involved in the collision growth and gave us the clue to retrieve collision kernels. On the contrary, we have no available information about the collisions of the droplets out of the range. This brought the idea that the size-bin with larger number of droplets has more information for retrieving collision kernels, and this idea is considered by the weighting matrix in (36). Disagreement in collision kernels among droplets with small number densities are not important, it was expected by design.

For collision kernels among same-sized droplets ($r_1 = r_2$), the *a priori* information of (32) is rewritten as

$$K_c(r, r)/(\lambda R^3) = k_t. \tag{48}$$

This explains that the normalized retrieved collision kernels are constant, and therefore, both Kc-L and Kc-NL are demonstrated by horizontal straight lines in figure 6. In contrast, the DNS data decreases with increasing the radius. Although the difference between the DNS and retrieved values increases as the radius deviates from the crossing point of about 40 μm (St = 4.1), the difference is small around the most frequent radius, r_{freq} (=39.0 μm) (St = 3.9). To discuss the retrieval errors quantitatively, we introduce the error metric E_{rr} defined as

$$E_{rr} = \left(\frac{[\text{retrieved } K_c] - [\text{reference } K_c]}{[\text{reference } K_c]} \right) \times 100, \tag{49}$$

where reference K_c means the collision kernels obtained from DNS. The absolute values of E_{rr} for Kc-L and Kc-NL at r_{freq} are as small as 11 % and 5.0 %, respectively, in figure 6. Those errors are much smaller than the 23 % error from the rough estimation discussed in the latter part of § 4.1. This confirms that the present inversion schemes can retrieve the collision kernels among droplets around the most frequent radius.

The reason for the continuous decrease of the collision kernel in the DNS data with r in figure 6 is attributed to the so-called accumulation effect (Sundaram and Collins, 1997, Wang et al., 2000). The turbulent collision is caused by the combined effect of the relative velocity between two colliding particles (the turbulent transport effect), and the local nonuniform particle distribution (the accumulation effect). The turbulent transport effect reaches a maximum at $\tau_p/T_e \approx 1$, whereas the accumulation effect at $\tau_p/\tau_\eta (= St) \approx 1$. As the radius increases from 20 μm to 80 μm in the horizontal axis in figure 6, the values of τ_p/T_e and St increase from 0.13 to 2.1 and from 1.0 to 16.6, respectively. The turbulent transport effect increases and then decreases in

this radius range, whereas the accumulation effect continuously decreases. Therefore, the continued decrease of the collision kernel in the DNS data is attributed to the decrease of the accumulation effect.

Figure 7 shows the collision kernels between different droplet sizes obtained by DNS together with those retrieved using the present inversion scheme. Here, we show the collision kernels between droplets with the radius of $r_1 = 40$ μm ($St_1 = 4.1$) and other sized droplets with radius r_2. Strictly speaking, r_1 was 40.4 μm not 40.0 μm in the retrieved data because the discretizations in radius were different between the DNS calculations and the inversions. The small inconsistency of 1 % in radius was neglected in this discussion. The horizontal axis shows the radius r_2 (St_2), and vertical axis shows the collision kernels normalized in the same way in figure 6. The DNS data shows a smooth curve with a local minimum at around $r_2 = 45$ μm ($St_2 = 5.2$). In contrast, the retrieved results shown by the solid line have discontinuity at $r_2 = 24.0$ and 66.7 μm (St_2=1.5 and 11.5, respectively) derived from the conditional statements in (33). To remove the discontinuity, the *a priori* information needs to be modified. Despite this shortcoming, retrieved values well agree with the DNS results around $r_2 = r_{freq}$. The average values of E_{rr} in (49) for Kc-L and Kc-NL, for example, in the range of $r_{freq} < r_2 < r_{ave}$ are as small as 4.7 % and 13 %, respectively.

The reason why the DNS data in figure 7 has the local minimum can be explained by the fact that the gravitational collision kernel, i.e., the hydrodynamic kernel expressed as (29) becomes dominant when the size difference becomes large. Using $V_\infty = g_r \tau_p$ and (45), (29) is rewritten as

$$K_{c,hydr}(r_1, r_2)/(\lambda R^3) = \left(\frac{2\pi g_r \rho_p}{9\nu\rho_f \lambda} \right) |r_1 - r_2| \,. \tag{50}$$

This equation explains that the normalized hydrodynamic kernel is proportional to the radius difference between colliding droplets, $|r_1 - r_2|$. The larger the value of $|r_1 - r_2|$ becomes, the larger hydrodynamic kernel becomes, which means that the gravitational contribution becomes more dominant in collisions. Therefore, the DNS data has a local minimum near $r_2 = 40$ μm ($St_2 = 4.1$), where $|r_1 - r_2| = 0$.

4.3. Reynolds number dependency of retrieval errors

Figure 8 shows collision kernels among same-sized droplets with a radius of 40 μm, which is almost equivalent to the most frequent radius, r_{freq}. The horizontal axis shows the turbulent Reynolds number based on the Taylor-microscale, Re_λ. Solid circles in figure 8 are the DNS data, while the open triangles and circles are the collision kernels retrieved by the linear (Kc-L) and nonlinear inversions (Kc-NL), respectively. Both the Kc-L and Kc-NL predict that the collision kernel increases with increasing the turbulent Reynolds number, but Kc-L shows smaller values than the DNS data, especially for high Reynolds numbers. In contrast, Kc-NL agrees well with the DNS data for all Reynolds numbers.

Figure 9 shows the retrieval errors, E_{rr}, against the turbulent Reynolds number, Re_λ. The vertical axis show the absolute value of E_{rr}. With increasing Re_λ, the retrieval error of Kc-L increases, while that of Kc-NL remains small. It is implicitly assumed, in the linear scheme, that the number of collisions is small and therefore, the size distribution does not change much for $\Delta T = 0.2$ s. This assumption leads to underestimate of kernel values to compensate the overestimate that $N(r_{freq}, t_0)^2 > (1/\Delta T) \int_{t_0}^{t_0+\Delta T} N(r_{freq}, t)^2 dt$. As a result, the linear scheme has less validity in higher Reynolds number

flows where the collision frequency is larger. Compared with the large error of Kc-L, the error of Kc-NL remains within 10 % in all flows.

4.4. C_t dependency of retrieval errors

In this paper, we use simple assumptions as (32) and (33) to linearlize the *a priori* information. The linear form enables us to perform linear inversion and to discuss the difference between linear and nonlinear schemes. However, it remains uncertain in the parameter C_t in (33).

Figure 10 shows the retrieval errors, E_{rr}, against C_t. Here it should be noted that gray color indicates positive E_{rr}, i.e., [retrieved K_c] > [reference K_c]. This figure clearly shows two features. One is that the linear inversion predicts smaller kernel values than the nonlinear one. This is because the linear scheme neglects the change in size distribution during the collision growth time ΔT. The other is that errors of both linear and nonlinear inversions increase rapidly as C_t decreases when $C_t < 0.2$. This means the turbulent collisions are dominant in $r^{\#}_{diff} < 0.2$ and the turbulent contribution term $k_t \lambda R^3$ in (32) must not be neglected there.

The value of C_t is a threshold to switch the dominant contribution to collision growth, i.e., whether the gravitational ($K_{c,hydr}$) or turbulent contribution ($k_t \lambda R^3$). Ideally, C_t should be determined depending on the target system since the turbulent contribution changes due to droplet size and flow condition. One may estimate the value of C_t from the value of $r^{\#}_{diff}$ with which the gravitational and turbulent contributions become equivalent: Equations $K_{c,hydr} = k_t \lambda R^3$ and $r^{\#}_{diff} = \frac{|r_i - r_j|}{(r_i + r_j)/2}$ yield

$$r_{diff}^{\#} = \frac{k_t \lambda}{R} \cdot \frac{9\nu\rho_f}{\pi g_r \rho_p}. \tag{51}$$

Substituting the value of k_t for r_{freq} droplets obtained from the DNS in FLOW-1,2,3 and 4 yields $r_{diff}^{\#}$ =0.56, 0.85, 1.1 and 1.3, where R is assumed to be $2r_{freq}$. This suggests $C_t = 1.3$ for FLOW-4. However, figure 10 shows that $C_t = 0.2$ and $C_t = 0.4$ provide better results for linear and nonlinear schemes, respectively. This means that we have better value of C_t than the estimate from (51). For example, our setting $C_t = 0.5$ provides good performance as in figure 9. This study does not start further discussion in searching better C_t for better retrieval. We think, it is more promising to use an assumption permitting both kernel components to play a role in the range where they have nearly equal affect. Utilizing equation (42) is one option. It leads to

$$K_c(r_1, r_2) = k_{t,1} R^3 \left((r_1 - r_2)^2 + k_{t,2} \right)^{1/2}, \tag{52}$$

where the two parameters $k_{t,1}$ and $k_{t,2}$ are to be determined. The current our schemes are not designed for retrieving multiple parameters and cannot be applied directly to this type of *a priori* information. However, a slight modification will make our schemes applicable to it. This will come in the next work.

4.5. Convergence of the present nonlinear scheme

We have shown that the nonlinear scheme is more reliable than the linear scheme particularly in higher Reynolds number flows. However, in general, it

is recognized that nonlinear schemes occasionally have problems on convergence and determination of the initial value. In the present nonlinear scheme, we set the acceleration coefficient, α, in (40) to 0.0005 and used the value obtained from the linear scheme, k_t^L, as the initial value of k_t, k_t^0. A smaller α makes it safer to converge, but requires more iterations. The closer value of k_t^0 is to the true value, the better for the convergence in nonlinear inversions. In general, if an unsuitable initial value is used, a nonlinear inversion may not find the converged value or in the worst case, it may find an incorrect converged value.

To investigate the convergence of the present nonlinear scheme, we performed the nonlinear inversion in FLOW-4 with different k_t^0 and α. Table 2 lists the obtained converged values. The word "NC" stands for "not convergent" within 10 000 iterations. Table 2 indicates that α should be less than 0.01, and k_t^L for k_t^0 is more robust in convergence than other arbitrary values. The converged values range from 23.4 to 23.8 when α is set to less than 0.001. The deviation in this range is as small as 1.7%, implying that the present nonlinear scheme has a single convergence value around the true value, and does not produce multiple convergence values. This is an important feature of the present nonlinear scheme, which is based on the simple *a priori* information in (32). Here, we discussed the results in FLOW-4, where the largest number of iterations is required due to the largest difference between k_t^L for the initial and the converged value among the four simulations. The other three simulations provided qualitatively similar results.

	α =0.0005	α =0.001	α =0.005	α =0.01	α =0.05
k_t^0 =1.0	23.7	23.4	23.4	NC	NC
k_t^0 =5.0	23.8	23.8	23.9	23.1	NC
k_t^0 =14.7 (= k_t^L)	23.6	23.8	24.3	23.2	NC
k_t^0 =50.0	23.6	23.8	NC	NC	NC
k_t^0 =100.0	23.7	23.8	NC	NC	NC

Table 2: Converged values of k_t in the nonlinear scheme with various k_t^0 and α in FLOW-4. NC stands for "not convergent" within 10000 iterations.

5. Conclusions

We have proposed original simple linear and nonlinear inversion schemes to retrieve collision kernel parameters from changes in droplet size distribution due to collision growth. Our schemes directly handle binned (discretized) size distributions and, therefore, do not require any assumptions on distribution forms, such as the self-similarity assumption commonly used in colloidal agglomeration researches. The self-similarity assumption is not a common way in measurements of inertia droplets in turbulent wind tunnel since the group of droplets goes out of the tunnel before achieving a similarity. Being free from the similarity assumption, our schemes are promising for retrieving collision frequencies from size measurements of inertia droplets in turbulent wind tunnel.

Three-dimensional direct numerical simulation (DNS) of particle-laden turbulent flows, where droplets grow due to geometric collisions, was performed in order to investigate the validity of our schemes. In the DNS, air turbulence was calculated using a pseudo-spectral method, while droplet

motions were tracked by the Lagrangian method. Sample data on the size distribution changes due to collision growth were obtained, and used as input to the retrieval schemes. Comparisons of the retrieved collision kernels with reference kernels obtained directly from the simulations show that kernels can be retrieved with good accuracy by both the linear and nonlinear inversion schemes in low Reynolds number flows. However, in higher Reynolds number flows the retrieval error becomes large for the linear scheme, while the error remains small for the nonlinear scheme. This verifies the feasibility of using the nonlinear scheme to derive collision kernels from measurements of the evolution of droplet size distribution.

Acknowledgments

This research was supported by a Grant-in-Aid from the Ministry of Education, Culture, Sports, Science and Technology (MEXT) of Japan for Young Scientists (B) 18760137, and was partially supported by Core Research for Evolutional Science and Technology (CREST) Program "Advanced Model Development and Simulations for Disaster Countermeasures" of Japan Science and Technology Agency (JST).

References

Abrahamson, J., 1975. Collision rates of small particles in a vigorously turbulent fluid. Chem. Eng. Sci. 30, 1371–1379.

Aliseda, A., Cartellier, A., Hainaux, F., Lasheras, J. C., 2002. Effect of preferential concentration on the settling velocity of heavy particles in homogeneous isotropic turbulence. J. Fluid Mech. 468, 77–105.

Bagchi, P., Balachandar, S., 2003. Effec of turbulence on the drag and lift of a particle. Physics of Fluids 15, 3496–3513.

Berry, E. X., 1967. Cloud droplet growth by collection. J. Atmos. Sci. 24, 688–701.

Berry, E. X., Reinhardt, R. L., 1974. An analysis of cloud drop growth by collection: Part 1. double distribution. J. Atmos. Sci. 31, 1814–1824.

Bleck, R., 1970. A fast approximate method for integrating the stochastic coalescence equation. J. Geophys. Res. 75, 5165–5171.

Bott, A., 1998. A flux method for the numerical solution of the stochastic collection equation. J. Atmos. Sci. 55, 2284–2293.

Davis, M. H., Sartor, J. D., 1967. Theoretical collision efficiencies for small cloud droplets in stokes flow. Nature 215, 1371–1372.

Dodin, Z., Elperin, T., 2002. On the collision rate of particles in turbulent flow with gravity. Phys. Fluids 14, 2921–2924.

Enukashvily, I. M., 1980. A numerical method for integrating the kinetic equation of coalescence and breakup of cloud droplets. J. Atmos. Sci. 37, 2521–2534.

Eyre, D., Wright, C. J., Reuter, G., 1988. Spline-collocation with adaptive mesh scheme grading for solving the stochastic collection equation. J. Comput. Phys. 78, 288–304.

Falkovich, G., Fouxon, A., Stepanov, M. G., 2002. Acceleration of rain initiation by cloud turbulence. Nature 419, 151–154.

Gelbard, F., Seinfeld, J. H., 1978. Numerical solution of the dynamic equation for particulate systems. J. Comput. Phys. 28, 357–375.

Ishioka, K., 2005. ispack-0.71, http://www.gfd-dennou.org/arch/ispack/. GFD Dennou Club 1, 1.

Jonas, P. R., Goldsmith, P., 1972. The collection efficiencies of small droplets falling through a sheared air flow. J. Fluid Mech. 52, 593–608.

Khain, A., Pinsky, M., Elperin, T., Kleeorin, N., Rogachevskii, I., Kostinski, A., 2007. Critical comments to results of invetigations of drop collisions in turbulent clouds. Atmos. Res. 86, 1–20.

Klett, J., Davis, M., 1973. Theoretical collision efficiencies of cloud droplets at small reynolds numbers. J. Atmos. Sci. 30, 107–117.

Kruis, F. E., Kusters, K. A., 1997. The collision rate of particles in turbulent flow. Chem. Eng. Comm. 158, 201–230.

Lin, C., Lee, S., 1975. Collision efficiency of water drops in the atmosphere. J. Atmos. Sci. 32, 1412–1418.

Muralidhar, R., Ramkrishna, D., 1986. An inverse problem in agglomeration kinetics. Journal of Colloid and Interface Science 112, 348–631.

Muralidhar, R., Ramkrishna, D., 1989. Inverse problems of agglomeration kinetics : II. binary clustering coefficients from self-preserving spectra. Journal of Colloid and Interface Sciences 131, 503–513.

Neizvestnaya, A. I., Kobzuenko, A. G., 1986. Effect of small-scale turbulence on the coagulation growth rate of cloud droplets. Izvestiya, Atmospheric and Oceanic Physics 22, 481–487.

Onishi, R., 2005. Numerical simulations of chemical reaction and droplet growth in environmental turbulent flows. Ph.D. thesis, Kyoto University, Kyoto, Japan.

Onishi, R., Komori, S., 2004. The collision rate of monodisperse particles in turbulent flows with gravity. Fifth Intl Conf. on Advances in Fluid Mechanics 5, 229–235.

Onishi, R., Matsuda, K., Takahashi, K., Kurose, R., Komori, S., 2008. Retrieval of collision kernels from the change of droplet size distributions with a simple inversion scheme. Physica Scripta T132, 014050.

Onishi, R., Takahashi, K., Komori, S., 2009. Influence of gravity on collisions of monodispersed droplets in homogeneous isotropic turbulence. Physics of Fluids 21, 125108.

Patra, P. K., Mikaloff-Fletcher, S. E., Ishijima, K., Maksyutov, S., Nakazawa, T., 2006. Comparison of co2 fluxes estimated using atmospheric and oceanic inversions, and role of fluxes and their interannual variability in simulating atmospheric co2 concentrations. Atmos. Chem. Phys. Discuss. 6, 6801–6823.

Pinsky, M. B., Khain, A. P., 2002. Effects of in-cloud nucleation and turbulence on droplet spectrum formation in cumulus clouds. Q. J. R. Meteorol. Soc. 128, 501–533.

Pruppacher, H. R., Klett, J. D., 1997. Microphysics of clouds and precipitation second ed. Kluwer Academic Publishers, Boston.

Raikar, N. B., Bhatia, S. R., Malone, M. F., Henson, M. A., 2006. Self-similar inverse population balance modeling for turbulently prepared batch emulsions: Sensitivity to measurement errors. Chemical Engineering Science 61, 7421–7435.

Ramkrishna, D., 2000. Population Balances: Theory and Applications to Particulate Processes in Engineering. Adademic Press, New York, NY.

Ramkrishna, D., Mahoney, A. W., 2002. Population balance modeling. promise for the future. Chemical Engineering Science 57, 595–606.

Riemer, N., Wexler, A. S., 2005. Droplets to drops by turbulent coagulation. J. Atmos. Sci. 62, 1962–1975.

Saffman, P. G., Turner, J. S., 1956. On the collision of drops in turbulent clouds. Journal of Fluid Mechanics 1, 16–30.

Shafrir, U., Neiburger, M., 1963. Collision efficiencies of two spheres falling in a viscous medium. J. Geophys. Res. 68, 4141–4147.

Shaw, R. A., 2003. Particle-turbulence interactions in atmospheric clouds. Annu. Rev. Fluid Mech. 35, 183–227.

Simmel, M., Trautmann, T., Tetzlaff, G., 2002. Numerical solution of the stochastic collection equation – comparison of the linear discrete method with other methods. Atmos. Res. 61, 135–148.

Squires, K. D., Eaton, J. K., 1991. Measurements of particle dispersion obtained from direct numerical simulations of isotropic turbulence. J. Fluid Mech. 226, 1–35.

Sundaram, S., Collins, L. R., 1997. Collision statistics in an isotropic particle-laden turbulent suspension. part 1. direct numerical simulations. J. Fluid Mech. 335, 75–109.

Tzivion, S., Feingold, G., Levin, Z., 1987. An efficient numerical solution to the stochastic collection equation. J. Atmos. Sci. 44, 3139–3149.

Tzivion, S., Reisin, T., Levin, Z., 1999. A numerical solution of the kinetic collection equation using high spectral grid solution: a proposed reference. J. Comput. Phys. 148, 527–544.

Tzivion, S., Reisin, T. G., Levin, Z., 2001. A new formulation of the spectral multi-moment method for calculating the kinetic collection equation: more accuracy with few bins. J. Comput. Phys. 171, 418–422.

Wang, L.-P., Wexler, A. S., Zhou, Y., 1998. Statistical mechanical descriptionand modelling of turbulent coagulations. Phys. Fluids 10, 2647–2651.

Wang, L.-P., Wexler, A. S., Zhou, Y., 2000. Statistical mechanical descriptionand modelling of turbulent collision of inertial particles. J. Fluid Mech. 415, 117–153.

Wang, L.-P., Xue, Y., Grabowski, W. W., 2007. A bin integral method for solving the kinetic collection equation. J. Comput. Phys. 226, 59–88.

Wilkinson, M., Mehlig, B., Bezuglyy, V., 2006. Caustic activation of rain showers. Phy. Rev. Lett. 97, 048501.

Williams, J. J. E., Crane, R. I., 1979. Drop coagulation in cross-over pipe flows of wet steam. J. Mech. Engng. Sci. 21, 357–360.

Wright, H., Ramkrishna, D., 1992. Solutions of inverse problems in population balances-i. aggregtion kinetics. Computers and Chemical Engineering 16, 1019–1038.

Zauner, R., Jones, A. G., 2000. Determination of nucleation, growth, agglomeration and disruption kinetics from experimental precipitation data: the calcium oxalate system. Chemical Engineering Science 55, 4219–4232.

Zhou, Y., Wexler, A. S., Wang, L. P., 2001. Modelling turbulent collision of bidisperse inertial particles. J. Fluid Mech. 433, 77–104.

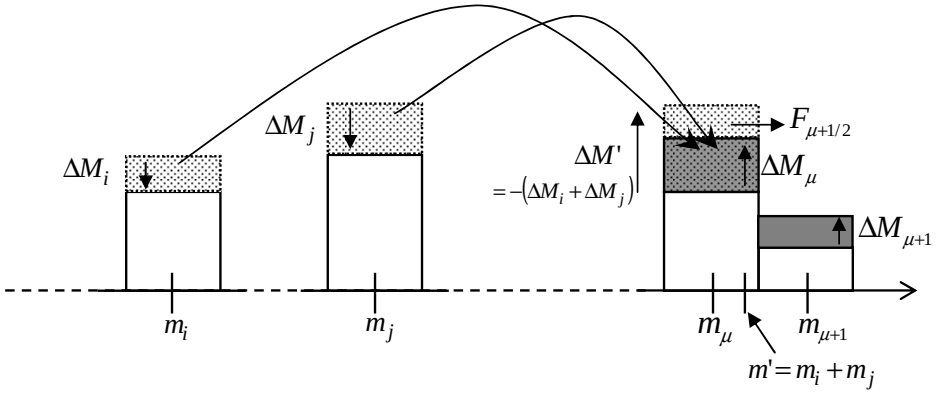

Figure 1: Schematic illustration of the upstream flux method of Bott (1998).

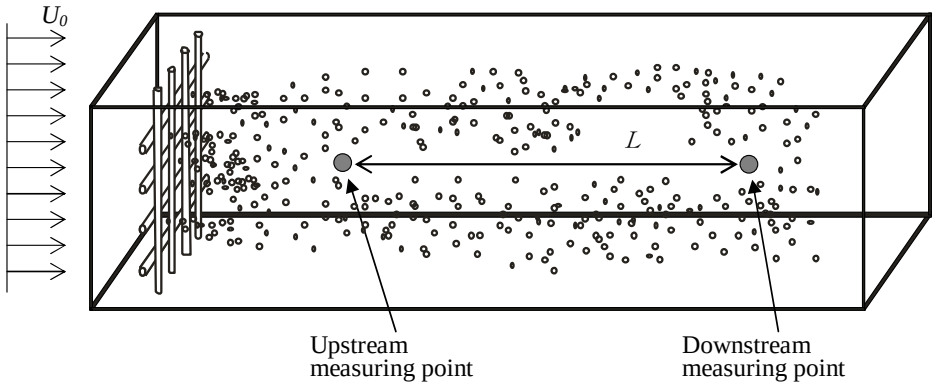

Figure 2: Schematic diagram of a plausible droplet collision experiment. Water droplets will be sprayed into a grid-generated isotropic turbulence. Size distributions of the water droplets will be measured at two different points to detect the difference between the two distributions generated by collision growth. This sketch shows a horizontal wind tunnel, where sprayed droplets sediment due to gravity. To exclude the effects of gravitational settling, a vertical wind tunnel is preferable.

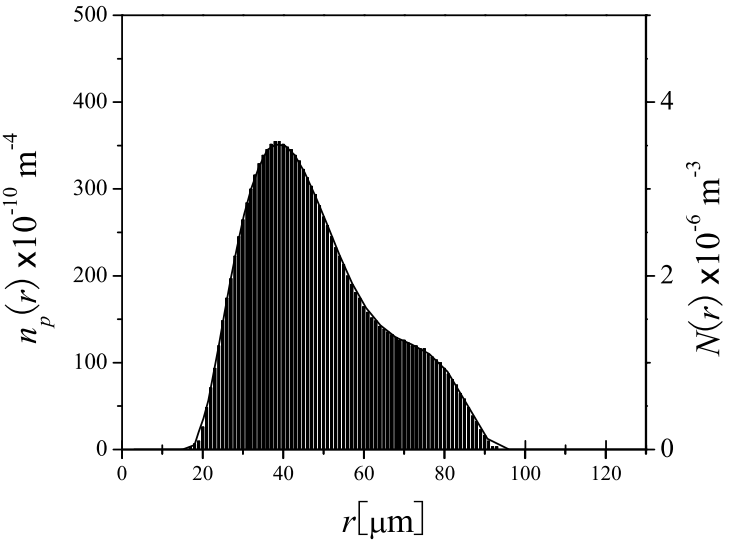

Figure 3: Droplet size distribution, $n_p(r)$, measured in a spray by a PDA. Most frequent radius, r_{freq}, in the size distribution is 39.0 μm, the number-average radius, r_{ave}, is 48.3 μm, and the standard deviation is 33.3 %. Initial number densities, $N(r)$, used for the DNS collision growth calculation are also drawn by bars. Left axis is for $n_p(r)$, and the right one is for $N(r)$.

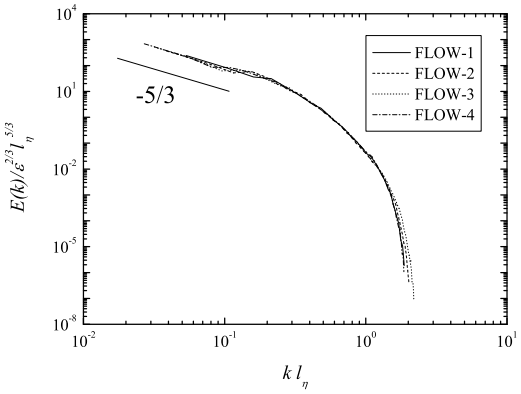

(a)

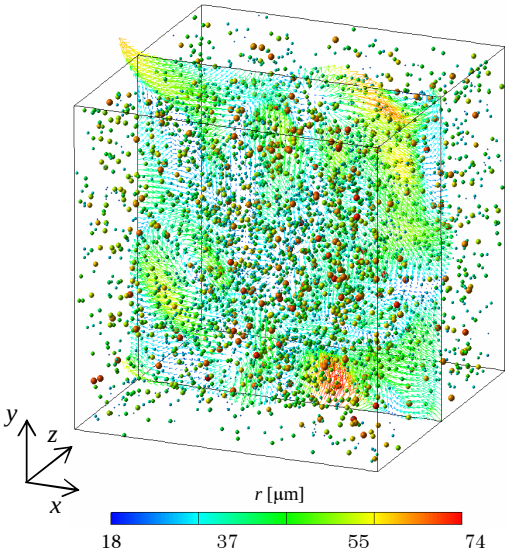

(b)

Figure 4: (a)Energy spectra of air turbulence. (b)Visualized three-dimensional velocity vectors on the plane of $z/L_0 = \pi$ and droplet positions in fully developed steady isotropic turbulence (FLOW-1). Droplet size is magnified by a factor of six for visualization purposes. The colour bar also shows the droplet size.

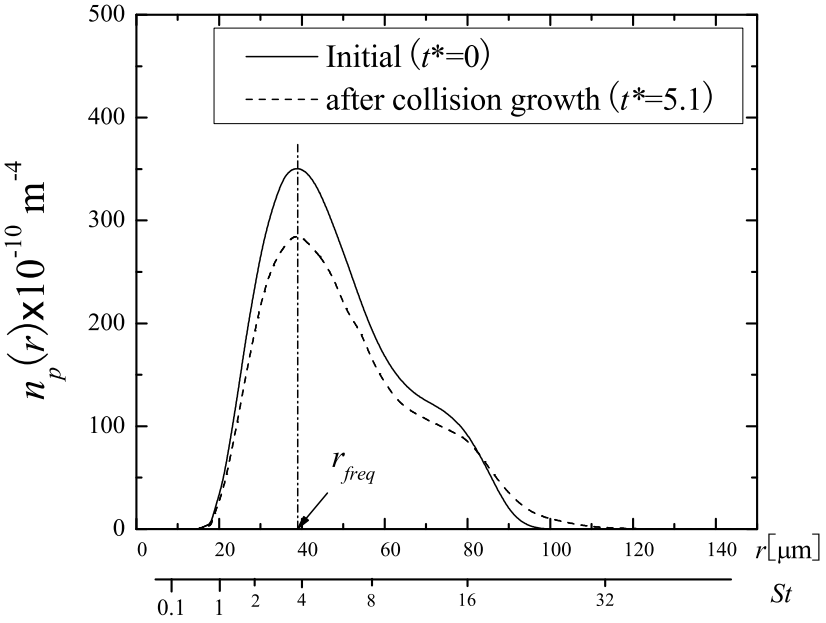

Figure 5: Change of droplet size distribution due to turbulent collision growth in FLOW-1: ——, initial (t^*=0); - - -, after collision growth (t^*=5.1).

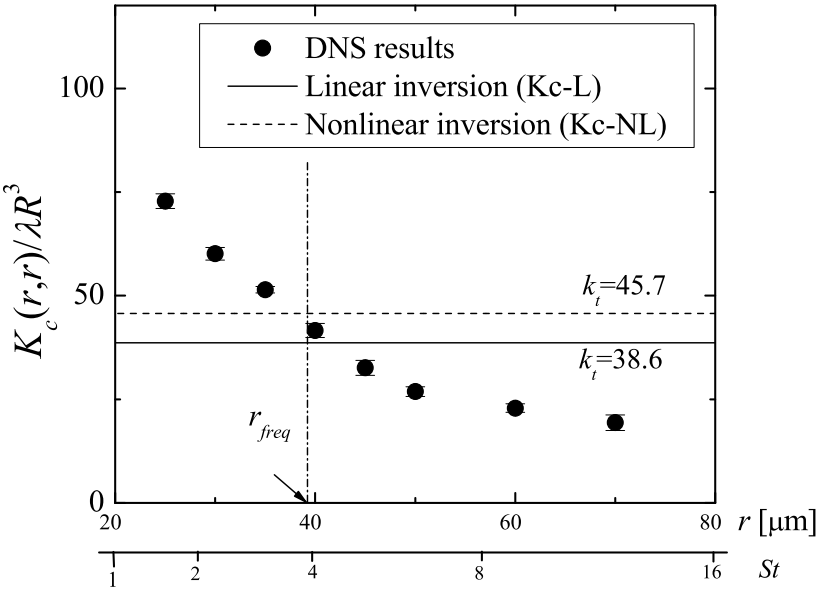

Figure 6: Normalized collision kernels between monodisperse droplets, $K_c(r,r)$, in FLOW-1: ● , DNS results; ——, Kc-L; - - -, Kc-NL.

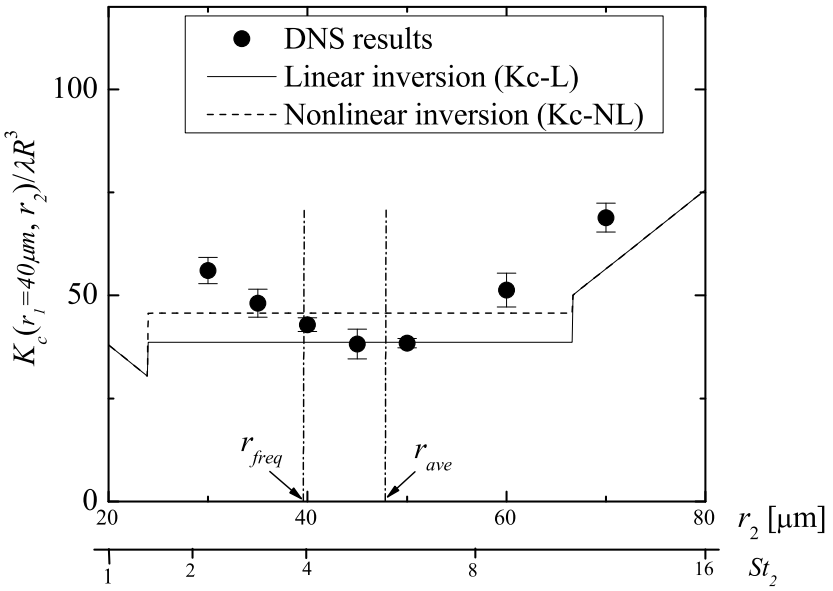

Figure 7: Retrieved collision kernels between droplets with the radius of $r_1 = 40$ μm, and droplets with radius of r_2, $K_c(40\ \mu\text{m}, r_2)$, in FLOW-1. Symbols as in figure 6.

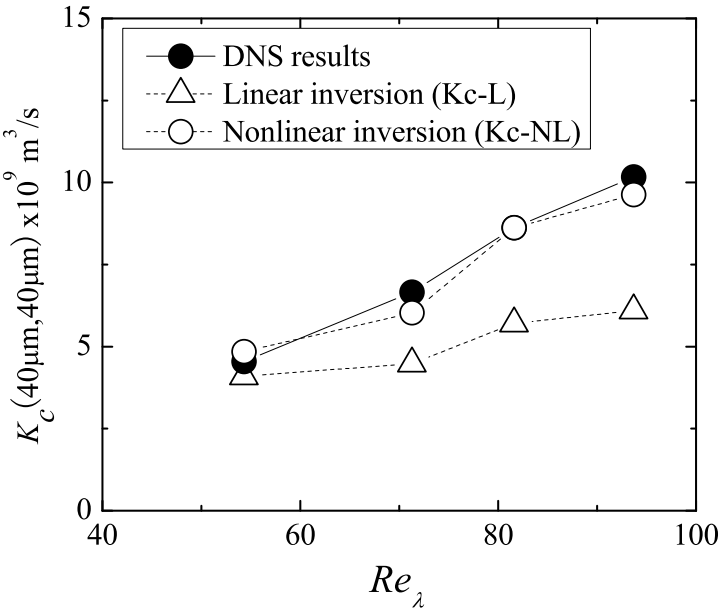

Figure 8: Normalized collision kernels among $r = 40$ μm droplets, $K_c(40\ \mu\text{m}, 40\ \mu\text{m})$, plotted against Re_λ: —●— , DNS results; --△--, Kc-L; --◯--, Kc-NL.

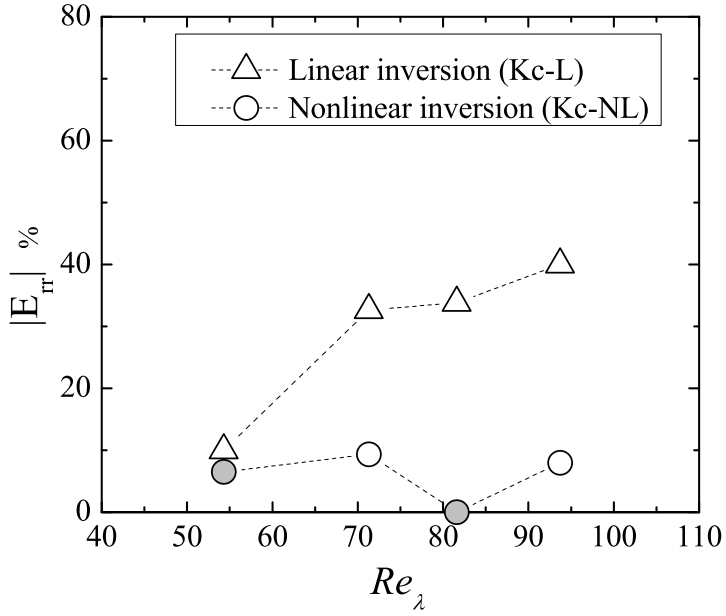

Figure 9: Retrieval errors, E_{rr} defined in (49), against Re_λ: --△-- , Kc-L; --◯--, Kc-NL. Gray color indicates positive E_{rr}, i.e., [retrieved K_c] > [reference K_c].

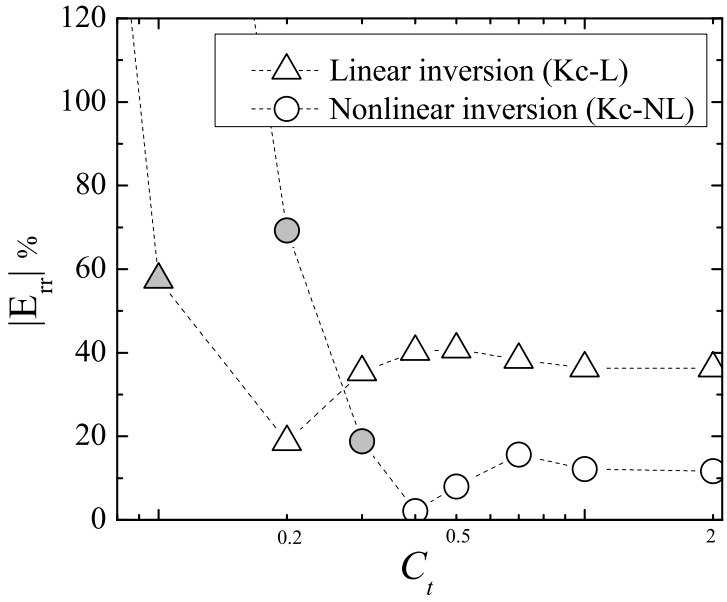

Figure 10: E_{rr} against C_t in FLOW-4. Symbols as in figure 9.